Study of Proton-Induced Defects in 40-nm CMOS SPADs

Ali Jouni, Victor Malherbe, Bastien Mamdy, Thomas Thery, Mathieu Sicre, Dimitri Soussan, Vincent Lorquet, Serge De Paoli, Jean-Marc Belloir, Valerian Lalucaa, et al.

Digital Object Identifier 10.1109/TNS.2023.3257740

Study of Proton-Induced Defects in 40-nm CMOS SPADs

Ali Jouni, *Student Member, IEEE*, Victor Malherbe, Bastien Mamdy, Thomas Thery, Mathieu Sicre, Dimitri Soussan, Vincent Lorquet, Serge De Paoli, Jean-Marc Belloir, Valérian Lalucaa, Cédric Virmontois, *Senior Member, IEEE*, Gilles Gasiot, *Senior Member, IEEE*, and Vincent Goiffon, *Senior Member, IEEE*

***Abstract*— Defects induced by 62 MeV protons in single-photon avalanche diodes (SPADs) are studied. A study of the dark count rate (DCR) variation after irradiations for different biasing conditions underlines the predominance of field enhancement effects such as Poole–Frenkel (PF) effect and phonon-assisted tunneling (PAT) over band-to-band tunneling (BTBT). Activation energy measurements below mid-gap value confirm the important contribution of these field effects. However, unexpected behaviors in these energies are seen: very low activation energies are extracted for SPADs with a DCR induced around 10^3 counts per second (cps). We attribute them to the contribution of different groups of defects, with different energy-level distribution. This analysis is completed with an annealing study between 100 °C and 300 °C. Results for high DCR SPADs correlate well with the presence of defect clusters. Moreover, histogram of the annealing temperature at which the DCR starts to drop displays two peaks at 170 °C and 250 °C. The first one is attributed to phosphorus vacancies and complex cluster of defects with an energy distribution inside the Si bandgap centered above mid-gap. The second one is attributed to clusters of divacancies that also anneal at temperatures around 250 °C.**

***Index Terms*— Band-to-band tunneling (BTBT), CMOS, dark count rate (DCR), defect clusters, displacement damage dose (DDD), divacancy, irradiation, isochronal annealing, P-V center, phonon-assisted tunneling (PAT), Poole–Frenkel (PF), proton, single-photon avalanche diode (SPAD).**

I. Introduction

SINGLE-photon avalanche diodes (SPADs) are p-n junctions biased above breakdown. They allow both single-photon sensitivity and high timing resolutions, which find interests for space applications. However, radiation coming from solar wind, Van Allen belts, or galactic cosmic rays and their interactions with SPAD sensitive areas must be studied. The goal is to predict the degradation of electrical parameters, such as SPAD dark count rate (DCR) during the time of the space mission. Nature of defects introduced by displacement damage dose (DDD) have been studied for years in silicon photodetectors and pixel arrays [1] and more specifically in CMOS image sensors (CIS) [2], [3]. Clusters of defects were identified: activation energy measurements revealed Shockley-read-hall (SRH) thermal generation as the main process altering the dark current. For irradiated SPADs, low mean activation energies were extracted [4], [5]. These values below mid-gap level are the signature of electric field enhancement (EFE) effects such as Poole–Frenkel (PF) effect and phonon-assisted tunneling (PAT) that increase the SRH generation rate [6].

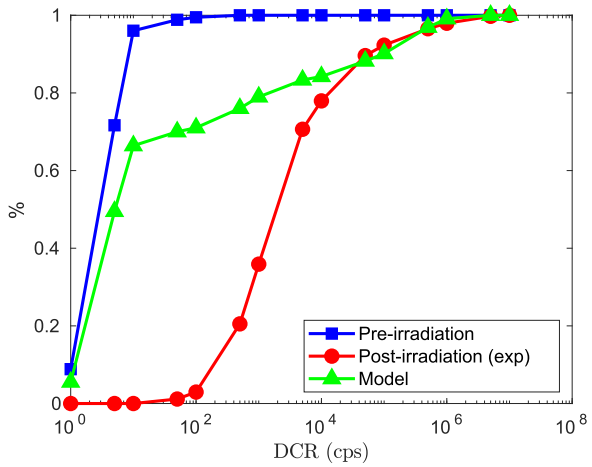

Fig. 1. DCR cumulative histogram of a 40-nm CMOS SPAD array irradiated using a proton fluence of 8.0×10^{10} p/cm^2. A model forecasting DCR increase with the proton dose presented in [7] is also superimposed.

However, the histogram of DCR increase after irradiations can be widely spread. In Fig. 1, the DCR cumulative distribution before and after proton irradiation at 8.0×10^{10} p/cm^2 is plotted. A Monte-Carlo simulation based on EFE equations, SPAD electrical properties, and the energy loss spectrum after proton-Si collisions is displayed. This model is detailed in [7]. The distribution of DCR increase can be explained by the correlation of two parameters. The first one is the defect complexity. According to the SRH theory [8], defects with energy states near mid-gap will induce the largest DCR increase. Moreover, the density of defects is directly proportional to the induce generation rate of carriers. Finally, a very dense cluster of poly-energy states can favor charge emission that increases the DCR degradation [9], [10]. This effect depends on the density of defects and the induced distribution of energy states.

The second parameter is the position of the damaged area inside the space charge region (SCR) and the avalanche region.

This work was supported in part by CNES, in part by STMicroelectronics, and in part by ISAE-SUPAERO.

Ali Jouni, Jean-Marc Belloir, Valérian Lalucaa, and Cédric Virmontois are with CNES, 31400 Toulouse, France (e-mail: ali.jouni@isae-supaero.fr).

Victor Malherbe, Bastien Mamdy, Thomas Thery, Mathieu Sicre, Dimitri Soussan, Vincent Lorquet, Serge De Paoli, and Gilles Gasiot are with STMicroelectronics, 38920 Crolles, France.

Vincent Goiffon is with the ISAE-SUPAERO, 31400 Toulouse, France.

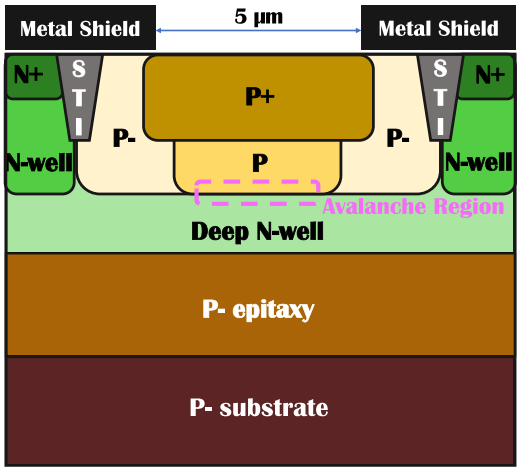

Fig. 2. Cross section of the irradiated SPADs [7], [11].

Indeed, if field enhancement effects as stated above are at play, the local value of the electric field will also have a significant effect on the DCR value. This second point was studied in [7] where PF effect and PAT equations were used to predict the DCR increase after proton irradiations considering the local electric field strength.

In this work, proton-induced defects in 40-nm CMOS SPAD arrays are further studied with the aim to identify their nature and their role in the DCR degradation. First, their field dependence is measured by increasing the voltage across SPADs. Then, activation energies between 10 °C and 25 °C are extracted and analyzed by comparing with results observed on proton-irradiated standard pixels with lower electric fields (below 10^5 V/cm). Finally, an isochronal annealing is performed between 100 °C and 300 °C to reveal the nature of these defects.

II. Description of SPADs and Irradiation Test Procedure

A. SPAD Description

SPADs used in this study are manufactured in a 40-nm CMOS technology by STMicroelectronics. Chips consist of 30 × 30 square SPADs with a pixel pitch of 7.8 μm. The sensitive area is a square of 25 μm^2 and it is formed by a p-over-n-junction (Fig. 2). The breakdown voltage of the arrays is reached at a measured voltage of about $V_{BD} = 14.0$ V at 25 °C. A spread of 0.1 V exists between SPADs of an array. A schematic of the pixel circuit is displayed in Fig. 3. A quenching transistor stops the avalanche and then resets the SPAD. Next, a NAND gate senses the voltage drop across the photodiode: a counter registers the number of triggering events during a certain amount of time, giving the number of cps. Before irradiation, the mean DCR of each chip was measured around tens of cps. More details about performances and pixel circuitry are given in [4], [11].

B. Irradiation Setup

Four SPAD chips were irradiated at "Université Catholique de Leuven" (UCL) in Belgium. A 62 MeV proton beam was used and fluences up to 1.0 × 10^{11} p/cm^2 were reached.

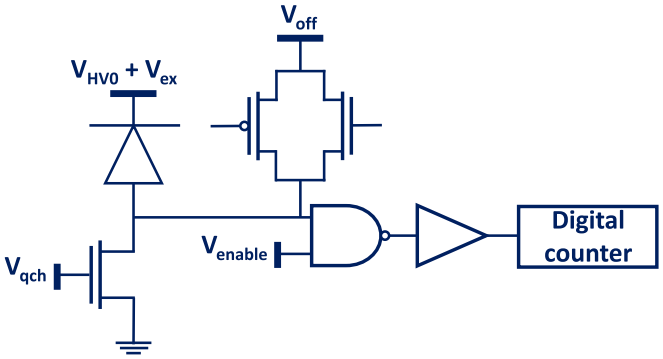

Fig. 3. Passive and readout circuit of the irradiated SPAD pixel. V_{ex} is the excess bias.

TABLE I
Detailed Design of Experiments

Device	#	Bias (V)	Proton Energy (MeV)	Fluence (p/cm^2)	DDD (TeV/g)
2D_SPAD1	1	$V_{HV0}+1$	56	2.0× 10^{10}	84.7
2D_SPAD2	1	$V_{HV0}+3$	56	2.0× 10^{10}	84.7
2D_SPAD3	1	0	62	8.0× 10^{10}	316
2D_SPAD4	1	0	62	1.0× 10^{11}	402

Passive irradiations (meaning that SPADs were grounded with all pin short circuited during the experiment) and active irradiations (meaning that SPADs were biased, operated and readout during the experiment) were performed. For active irradiations, a 5 mm rigid polyvinyl chloride (PVC) cap was placed in front of the chips to do acquisitions in dark conditions. This PVC lowered the proton energies to 56 MeV. Table I regroups the details about the design of experiments of the irradiation tests. V_{HV0} is the addition of the breakdown voltage V_{BD} with the minimum voltage drop required by the NAND gate (0.6 V) to detect a pulse.

III. Results: Voltage Dependence and Activation Energies

A. Bias Dependence of Defects

After irradiation, we observed that most of the damaged SPADs have a DCR increasing exponentially with the excess bias (consistent with PF effect and PAT equations [7]). Thereby, we can express the DCR by introducing an exponential factor α

$$\mathrm{DCR}(V_{ex}) \propto \exp(\alpha \times V_{ex}) \quad (1)$$

with V_{ex} the excess bias added to V_{HV0}. The DCR is modulated by the breakdown probability P_{BP} for an electron-hole pair to trigger an avalanche. It also depends on V_{ex}. Therefore, we decided to remove the contribution of P_{BP} by performing acquisitions in dark and light conditions. In fact, in dark conditions, we have a DCR that depends on P_{BP} through

$$\mathrm{DCR}(V_{ex}) = P_{BP} \times U(V_{ex}) \quad (2)$$

with $U(V_{ex})$ the SRH generation rate introduced by a defect. Here, we neglect the contribution of afterpulsing in the total

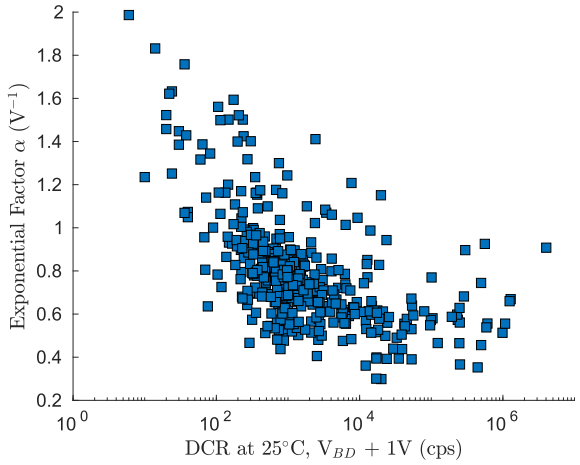

Fig. 4. Exponential factor of the DCR increase with excess bias measured at 10 °C. The x-axis corresponds to the related pixel DCR at 25 °C and 1 V excess bias (proton fluence: 1.0×10^{11} p/cm^2).

DCR. If SPADs are illuminated with a source of uniform flux Φ, the resulting light count rate (LCR) can be written as the DCR added to counts generated by light

$$\mathrm{LCR}(V_{\mathrm{ex}}) = \mathrm{DCR}(V_{\mathrm{ex}}) + P_{\mathrm{BP}}(V_{\mathrm{ex}}) \times \mathrm{QE} \times \Phi \tag{3}$$

with QE the quantum efficiency. Here, we assume that P_{BP} has a small variation over the depletion region. It means that P_{BP} only depends on the excess voltage V_{ex} and not on the defect position. Now, the normalized DCR for each V_{ex} can be computed to remove P_{BP} by using (2) and (3)

$$\mathrm{DCR}_{\mathrm{norm}}(V_{\mathrm{ex}}) = \frac{\mathrm{DCR}}{\mathrm{LCR} - \mathrm{DCR}} = \frac{U(V_{\mathrm{ex}})}{\mathrm{QE} \times \Phi}. \tag{4}$$

By doing so, the variation of the normalized DCR with V_{ex} is characterized only by the variation of the generation rate U.

In Fig. 4, we plot the coefficient α for all pixels after the irradiation at 1.0×10^{11} p/cm^2 measured at 10 °C versus the induced DCR at 25 °C and 1 V above V_{HV0}. For this purpose, we performed dark and light acquisitions to compute $\mathrm{DCR}_{\mathrm{norm}}$. Then, we injected $\mathrm{DCR}_{\mathrm{norm}}$ in (1) and we extracted α. LCR was measured using a 950 nm laser diode delivering a uniform flux over the SPAD array. This flux was such that the average LCR over the array was at 2.23×10^6 cps in illumination conditions. Moreover, for both dark and light acquisitions, all SPADs were not enabled at the same time to avoid crosstalk.

We notice in Fig. 4 that α falls progressively when the induced DCR increases. According to technology computer-aided design (TCAD) simulations in the range of V_{ex} between 1 and 3 V, the electric field increases nearly uniformly inside the depletion region. It means that the defect position inside the SCR cannot explain this large decrease in α with an increasing DCR. However, the progressive predominance of PF effect and PAT over band-to-band tunneling (BTBT) can explain this variation of α with the induced DCR. In fact, BTBT is not caused by proton-induced defects. Furthermore, for the electric fields involved, the induced generation rate is lower for BTBT than PF and PAT effects but the increase with the excess bias is faster [12]. Therefore, SPADs in Fig. 4 with a high value of α are dominated by BTBT and the higher the DCR, the higher the dominance of PF and PAT over BTBT.

B. Activation Energies

We extracted activation energies E_a between 10 °C and 25 °C to study proton-induced defects. The reason of this narrow range of temperature is that relatively low DCR SPADs at 25 °C (around hundreds of cps at this temperature) will have a DCR below the sensitivity of measurement if the temperature drops below 10 °C. Above 25 °C, diffusion current start to be significant for these low DCR SPADs and annealing can start for high DCR SPADs.

The activation energy describes how the DCR increases with temperature

$$\mathrm{DCR} \propto \exp\left(-\frac{E_a}{k_B.T}\right) \tag{5}$$

E_a depends on the trap energy E_T of the defect in the Si bandgap. T is the SPAD temperature and k_B the Boltzmann's constant. If we only consider defects in the SCR, equal capture cross sections for electrons and holes and no EFE effects, we can estimate E_a

$$E_a \approx 0.63 \text{ eV} + |E_T - E_i| \tag{6}$$

with E_i the mid-gap energy value (0.56 eV). The term 0.63 eV is the empirical value measured for hot pixels [2], [3]. It slightly differs from the analytical value of 0.65 eV that takes into account the energy transition from mid-gap to the conduction or valence band, the T^2 dependence of the generation rate U and the thermal variation of the bandgap [13]. Furthermore, under the same assumptions, the thermal generation rate U can be approximated [8]

$$U \propto \frac{1}{\cosh\left(\frac{E_T - E_i}{k_B.T}\right)}. \tag{7}$$

The more E_T is close to E_i (meaning $E_a = 0.63$ eV), the higher the induced U and the DCR. This is observed with standard pixels with low electric fields (below 10^5 V/cm). In Fig. 5, we give the average behavior of E_a depending on the induced dark current for CIS pixels. This plot is based on the results of [3] where E_a is extracted between -8 °C and 22 °C and after a proton fluence of 10^{12} p/cm^2. Slow increase in dark current corresponds to activation energies between 0.90 and 0.70 eV. In [3], divacancies (V_2) were attributed to these defects which is consistent with other studies after neutron irradiations [9]. E_a between 0.9 and 0.63 eV could be other complex defects with an induced energy-level distribution centered above mid-gap [14]. Finally, for higher dark current increases, activation energies around 0.63 eV corresponding to mid-gap levels were attributed to the presence of defect clusters with an energy state distribution centered around mid-gap.

For SPADs, as described in Section III-A, PF and PAT must be considered. Equations governing these EFE effects are described in [7]. High electric fields will induce an increase of U (and thus of the DCR) by a factor EF and a drop in E_a that will depend on the local electric field strength [6]. Numerical simulations based on the model presented in [7] allow us to compute the theoretical activation energy decrease depending on the local electric field. By computing PF and PAT equations as done in [7], a maximum drop of 0.18 eV is expected at the

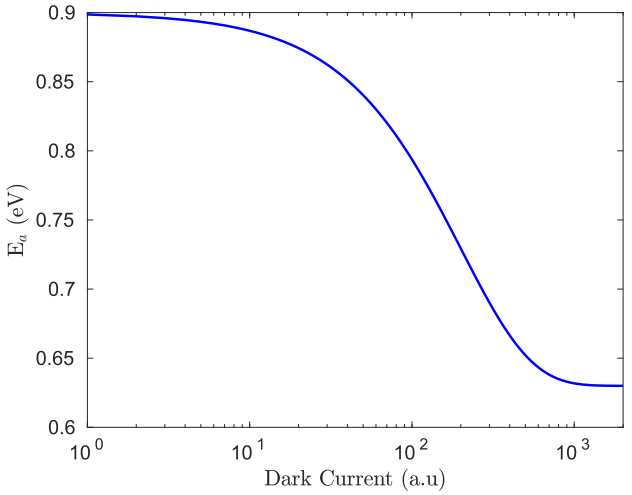

Fig. 5. Average behavior of activation energies depending on the induced dark current of irradiated standard pixels (plot based on results given in [3], logarithmic scale in the x-axis).

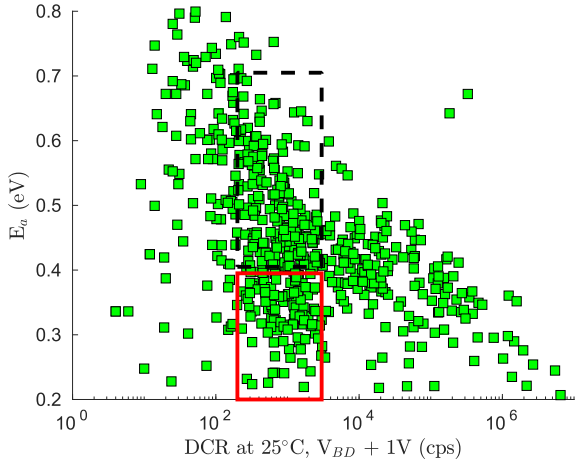

Fig. 6. Activation energies of irradiated SPADs at 1.0×10^{11} p/cm^2 extracted between 10 °C and 25 °C at $V_{\mathrm{HV0}} + 1$ V, depending on the induced DCR at 25 °C and $V_{\mathrm{HV0}} + 1$ V (logarithmic scale in the x-axis).

center of the SCR, where the factor EF is also extremely high. For lower electric fields, this decrease of E_a is less important. Therefore, we expect that the shape observed in Fig. 5 will extend in the y-axis and shifted toward lower energies.

Experimental activation energies Ea were extracted for SPADs between 10 °C and 25 °C. They are plotted in Fig. 6 as a function of the DCR measured at 25 °C and at an excess bias of 1 V. Pre-irradiation DCR of SPADs was below 200 cps in these conditions. We will thus focus on SPADs with post-irradiation DCR above 200 cps. In this figure, activation energies below the mid-gap value are measured, which is consistent with the predominance of EFE effects. However, the shape observed differs from what was forecast above. Indeed, a high density of points where the DCR is around 10^3 cps have an E_a below 0.40 eV (solid rectangle in Fig. 6), which is lower than the activation energy of SPADs with DCR between 4×10^3 cps and 10^5 cps. These unexpected low E_a at low DCR were also observed in standard pixels with high electric fields [6]. Furthermore, for this population of SPADs in this solid box and for pixels with DCR higher than 10^5 cps, the E_a is too low compared to the predicted drop of E_a using PF and PAT equations. We will see in the annealing study that these SPADs below 0.40 eV in the solid rectangle can be distinguished from those with higher E_a (dashed rectangle) by their characteristic annealing temperatures. The SPAD responses in the dashed rectangle were expected and correspond to defects with higher energy states than mid-gap value. As mentioned above, V_2 and other clusters with an energy distribution centered above mid-gap can be attributed to these pixels. Another possible contribution of this large spread in E_a for DCR around 10^3 cps is the uncertainty related to the narrow range of temperature in which activation energies are extracted.

For SPADs with DCR above 10^4 cps, E_a decreases and seems to converge toward 0 eV. As mentioned above, these pixels are probably affected by clusters of defects with an energy state distribution centered at mid-gap. These defect pockets induce a large number of energy states in the Si bandgap compared to isolated point defects [14]. They are also observed with standard pixels with low and high electric fields. The reason of very low activation energies for high DCR SPADs may be found in studies about defect clusters. In [14], authors distinguished PF effect and PAT due to the applied electric field (extrinsic contribution) from these EFE effects due to the abrupt heterojunction between amorphous silicon a-Si and c-Si (intrinsic contribution). This intrinsic part depends on the cluster size, its geometry, and the electric field. Therefore, the higher this contribution, the lower the activation energy. Bandgap narrowing due to local dilatation induced by heavy amorphous clusters could also be responsible for lowered Ea [15].

Finally, we looked at the effect of biasing conditions on E_a computed between 10 °C and 25 °C. At $V_{\mathrm{HV0}} + 3$ V, for hit pixels (with post-irradiation DCR higher than 200 cps), the mean E_a decreases from 0.41 to 0.35 eV compared to data at $V_{\mathrm{HV0}} + 1$ V. This was expected because PF and PAT increased which means that E_a is lowered. However, we noticed that for high-induced DCR, the decrease in E_a is less important, which is consistent with the assumption of an intrinsic contribution of the amorphous pocket.

IV. Isochronal Annealing: Results and Discussions

An efficient method to identify or characterize defect natures is by performing a thermal isochronal annealing. Depending on their nature, isolated point defects and clusters start to anneal at different characteristic temperatures [9], [14], [16]. In this work, such annealing has been performed on SPADs irradiated at 1.0×10^{11} p/cm^2. We have swept the temperature between 100 °C and 300 °C. After 130 °C, we chose a 20 °C step to 270 °C and finished with a final annealing at 300 °C. Each step lasted 30 min, as previously done in other studies [3], [13]. Finally, we have measured the DCR of SPADs after each stage at 25 °C and $V_{\mathrm{HV0}} + 1$ V.

A. Mean and Median DCR After Isochronal Annealing

We plot in Fig. 7 the mean and median DCR of the annealed chip. An important decrease of more than a decade is observed

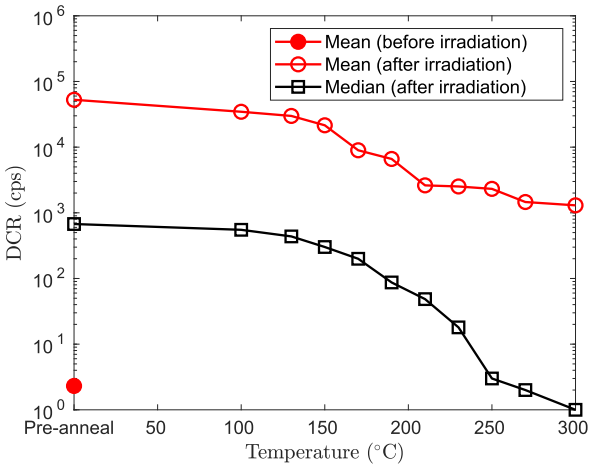

Fig. 7. Mean and median DCR after each annealing step performed on SPADs irradiated at 1.0×10^{11} p/cm^2. The median DCR before irradiation was measured at 0 cps.

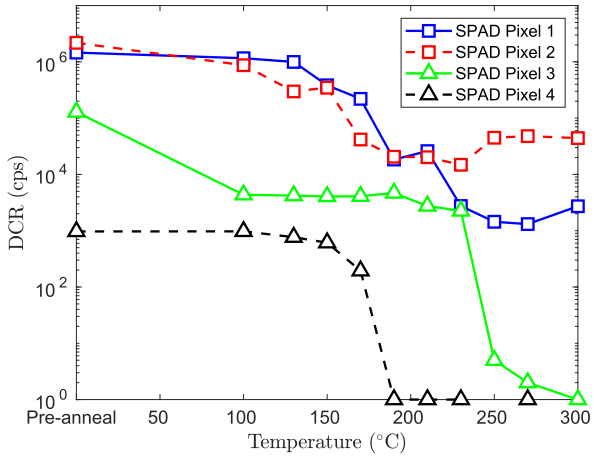

Fig. 8. Example of different annealing behaviors observed on four pixels (proton fluence: 1.0×10^{11} p/cm^2). For these SPADs, DCR before irradiation was measured at 0 cps for each SPAD.

between 150 °C and 300 °C for the average DCR. It mainly corresponds to the recovery of high DCR SPADs that dominate the mean DCR. At the end of the annealing procedure, the average DCR is around 10^3 cps, which is always higher than the pre-irradiation value (tens of cps). It means that high DCR SPADs do not completely recover. On the other hand, the median DCR decreased by three decades, starting at 150 °C like the mean, and reached the pre-irradiation value at the end of the annealing procedure. It corresponds to the full recovery of low and medium DCR SPADs (up to 10^5 cps before the annealing).

The analysis performed on the average and the median DCR after annealing can be completed by looking at the behavior of each SPAD. In Fig. 8, we plot the DCR after each annealing step for four SPADs. Different annealing behaviors can be noticed. In this figure, SPAD pixels 1 and 2 show a continuous decrease starting, respectively, after the step at 100 °C. Both SPADs have partially recovered after the last annealing step. It illustrates perfectly well the conclusions made on the mean and median DCR. On the other hand, a very sharp decrease is observed for SPAD pixels 3 and 4 after the 250 °C and 190 °C steps, respectively. At the end of the annealing procedure, the DCR of these two SPADs reaches the pre irradiation DCR that was measured at 0 cps.

Therefore, different groups of SPADs must be distinguished for the annealing analysis: the high DCR SPADs (with a DCR higher than 10^5 cps at 25 °C and $V_{\mathrm{HV0}} + 1$ V), on the one hand, and the low DCR SPADs (with a DCR lower than 10^5 cps at 25 °C and $V_{\mathrm{HV0}} + 1$ V), on the other hand.

B. Annealing of High DCR SPADs (DCR $\geq 10^5$ cps)

For high DCR pixels, we have previously noticed that the annealing seems to start at the end of the 100 °C step. This statement is confirmed in the histogram of annealing temperatures for this group of pixels in Fig. 9. The annealing temperature corresponds to the step after which the DCR drops by 30% of its initial value. We interpreted this result by the dominance of defect clusters in this high DCR SPAD group. Indeed, it is consistent with other annealing studies of such

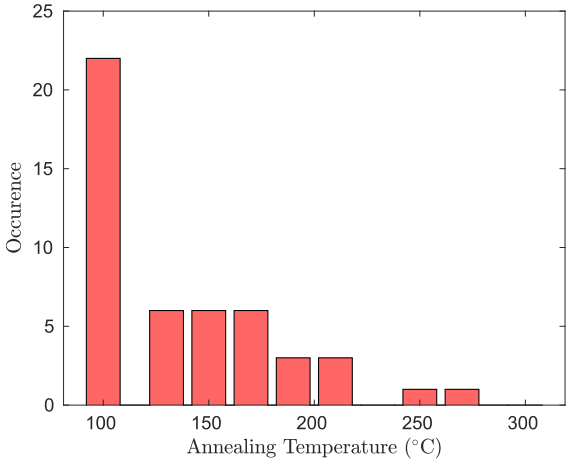

Fig. 9. Temperatures at which a 30% decrease of the DCR occurs for SPADs with a pre-annealing DCR higher than 10^5 cps.

defects [9], [14], [16]: these large clusters are expected to anneal in a progressive way, by eradicating a defect state or by changing its energy state distribution inside the bandgap. Furthermore, the high DCR induced by these defects suggest that most of them are located at the center of the SCR where EFE effects are stronger. One of the most common defect cluster is the cluster of divacancies that is expected by molecular dynamics and k-ART simulations [17], [18]. However, as the large majority of clusters starts to anneal at 100 °C or below, it is hard to conclude on the exact nature proton-induced clusters.

C. Annealing of Low DCR SPADs (DCR $< 10^5$ cps)

For low and medium DCR pixels, a sharper decrease at different temperatures is nearly always observed, the same way as SPAD 3 and 4 in Fig. 8. The histogram presented in Fig. 10 regroups the annealing temperatures after which an abrupt decrease occurs for SPADs with DCR between 200 cps and 10^5 cps. The criterion defining an abrupt decrease was chosen as follows: the DCR must fall by more than two decades from its initial value after two successive annealing steps. For example, the bin at "100 °C" means that some SPAD

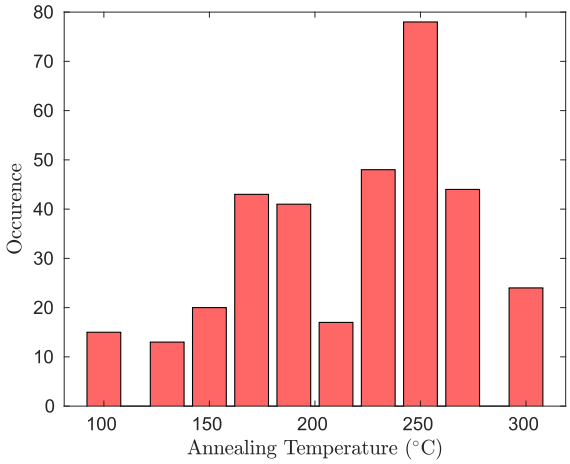

Fig. 10. Temperatures at which an abrupt DCR decrease occurs for SPAD with post-irradiation DCR below 10^5 cps.

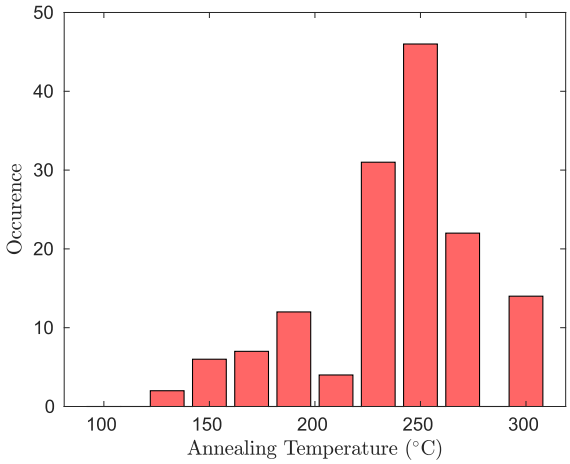

Fig. 11. Temperatures at which an abrupt DCR decrease occurs for SPADs inside the dashed rectangle in Fig. 6.

DCRs have decreased by two decades or more after the 100 °C step and the following one (130 °C). In Fig. 10, we observe two distinct peaks at 170 °C and 250 °C. The last one can be attributed to divacancies that start to anneal around this temperature [16]. It is consistent with our previous analysis of E_a when we observed a high density of SPADs with a medium and low DCR and activation energies higher than SPADs with higher DCR (dashed box in Fig. 6). We attributed this behavior to defects with higher energy states than clusters that have mid-gap energies. The energy state of the divacancy V_2 inducing the higher DCR increase has a value around 0.70 eV, which is consistent.

To confirm this assumption, we looked at the abrupt annealing only for the pixels inside the dashed box in Fig. 6. If our assumption of V_2 defect stands, it must be associated with SPADs in this dashed rectangle, with the higher E_a due to the associated trap level that is higher than mid-gap. In Fig. 11, we draw the distribution of abrupt annealing temperatures for these pixels in the dashed area in Fig. 6. We see a peak at 250 °C: this matches perfectly with our analysis and the fact that V_2 is involved.

For SPADs in the solid box in Fig. 6, the annealing temperature histogram is plotted in Fig. 12. This time, the peak

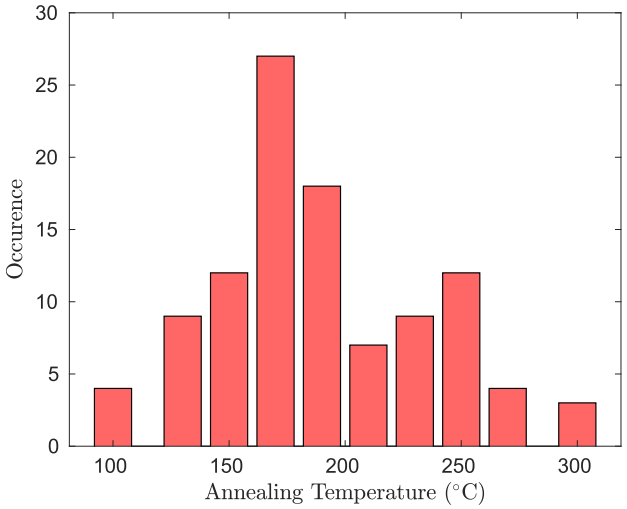

Fig. 12. Temperatures at which an abrupt DCR decrease occurs for SPADs inside the solid rectangle in Fig. 6.

observed around 170 °C in Fig. 10 appears for this category of SPADs. The phosphorus vacancy (P–V center) has an annealing temperature corresponding also to 170 °C [16]. Moreover, without EFE effects, the P–V center induces approximately the same dark current increase as V_2 [3], [10]. Therefore, it could be associated with SPADs in the solid rectangle in Fig. 6. In that case, the fact that the associated activation energies differ from divacancies in high electric field regime may be due to different interactions of defects with the field. Indeed, both defects can be either charged or neutral. Therefore, we can expect different influence of the electric field on these defects.

However, defect clusters with an energy distribution close to mid-gap but located in lower electric field regions than at the center of the SCR can also be attributed to these SPADs in the solid box in Fig. 6. In fact, first, clusters as multivacancy are known to anneal around this temperature [9]. Furthermore, according to PF and PAT equations and for the involved electric fields in this study, a factor of 10^3 on the induced DCR exists between a defect located at the center of the SCR and one at the edge [7]. In Section IV-B, we saw that high DCR pixels above 10^5 cps must be clusters of defects and they are probably located near the center of the SCR. Thereby if same defects are at the edge of the depletion region, PF and PAT equations predict an induced DCR between 10^2 cps and 10^3 cps, consistent with the range of DCR inside the solid box in Fig. 6. Moreover, it is also in line with the very low E_a for these SPADs. In fact, we mentioned EFE effects on the complex heterostructure between c-Si and a-Si that lower the E_a and depends only on the cluster geometry (intrinsic contribution of the defect). Therefore, it is not surprising to notice same E_a values between the low DCR SPADs in the solid box and high DCR SPADs. Finally, we also noticed a small peak in Fig. 12 at 250° C, meaning that V_2 defects are also present in this SPAD category.

A recap of this isochronal annealing is given in Table II, where defects are attributed depending on the induced DCR increase. The case of medium DCR SPADs was not specifically studied in this section because the corresponding

TABLE II

DEFECT ATTRIBUTION STUDY AFTER ISOCHRONAL ANNEALING DEPENDING ON THE INDUCED DCR AT 25 °C AND $V_{HV0} + 1$ V

		Induced DCR increase (cps)	Main Defect Attribution
High DCR SPADs		$\geq 10^5$	Large Clusters at the center of the SCR
Medium DCR SPADs		[3000, 10^5]	P-V center Clusters Divacancies
Low DCR SPADs	Dashed Rect. (Fig. 6)	[200, 3000]	Divacancies
	Solid Rect. (Fig. 6)	[200, 3000]	P-V center Clusters in low field regions

annealing temperature histogram looks like the one in Fig. 10. It means that P-V centers, clusters of defects, and divacancies can be attributed to these pixels.

V. CONCLUSION

In this work, the behavior of proton induced defects in 40-nm CMOS SPADs are studied. The electric field dependence of the induced DCR is measured: an exponential growth of the DCR with the excess bias is observed, which was expected with PF and PAT equations. The exponential rate α decreases with the induced DCR, showing the progressive domination of these EFE effects over BTBT. A study of activation energies E_a is also performed. A decrease in E_a compared to standard pixels with low electric fields has been observed and confirms the dominant contribution of PF and PAT. However, unexpected and extremely low activation energies are seen for SPADs with DCR around 10^3 cps and for very high DCR above 10^5 cps. The latter observation is directly attributed to clusters of defects that lowers the E_a due to deformation of the silicon band structure induced by amorphous pockets. An annealing study confirms this analysis with starting annealing temperatures measured mainly at 100 °C and a DCR that decreases continuously. Around 10^3 cps, abrupt annealing of SPADs with E_a higher than 0.40 eV shows a peak at 230 °C. This behavior has been attributed to divacancies inside these pixels. For the unexpected lower activation energies around the same induced DCR, histogram of annealing temperatures underlines a peak centered at 150 °C. The phosphorous vacancy has been identified but defect clusters such as multivacancies located in lower electric field areas in the SCR are also probable. More studies are still needed to have a complete understanding of proton-induced defects. For example, it would be valued to consider the effect of the defect charge state on the bias dependence, the activation energy, or the annealing temperature. This could be done by performing DLTS measurements and simulations.

ACKNOWLEDGMENT

The authors would like to thank Université Catholique de Leuven (UCL) for the use of the proton beam line and their assistance during irradiations.

REFERENCES

[1] J. R. Srour, C. J. Marshall, and P. W. Marshall, "Review of displacement damage effects in silicon devices," *IEEE Trans. Nucl. Sci.*, vol. 50, no. 3, pp. 653–670, Jun. 2003.

[2] C. Virmontois et al., "Displacement damage effects due to neutron and proton irradiations on CMOS image sensors manufactured in deep submicron technology," *IEEE Trans. Nucl. Sci.*, vol. 57, no. 6, pp. 3101–3108, Dec. 2010.

[3] J. M. Belloir et al., "Dark current spectroscopy in neutron, proton and ion irradiated CMOS image sensors: From point defects to clusers," *IEEE Trans. Nucl. Sci.*, vol. 64, no. 1, pp. 27–37, Jan. 2017.

[4] V. Malherbe, S. De Paoli, B. Mamdy, G. Gasiot, and P. Roche, "Displacement damage characterization of CMOS single-photon avalanche diodes: Alpha-particle and fast-neutron measurements," *IEEE Trans. Nucl. Sci.*, vol. 68, no. 5, pp. 777–784, May 2021.

[5] M. Campajola, F. Di Capua, D. Fiore, C. Nappi, E. Sarnelli, and L. Gasparini, "Long-term degradation study of CMOS SPADs in space radiation environment," in *Proc. 18th Eur. Conf. Radiat. Effects Compon. Syst. (RADECS)*, Gothenburg, Sweeden, Sep. 2018, pp. 87–91.

[6] J. R. Srour and R. A. Hartmann, "Enhanced displacement damage effectiveness in irradiated silicon devices," *IEEE Trans. Nucl. Sci.*, vol. 36, no. 6, pp. 1825–1830, Dec. 1989.

[7] A. Jouni et al., "Proton-induced displacement damages in 2D and stacked CMOS SPADs: Study of dark count rate degradation," *IEEE Trans. Nucl. Sci.*, early access, Feb. 23, 2023, doi: 10.1109/TNS.2023.3248521.

[8] C.-T. Sah, R. N. Noyce, and W. Shockley, "Carrier generation and recombination in p-n junctions and p-n junction characteristics," *Proc. IRE*, vol. 45, no. 9, pp. 1228–1243, Sep. 1957.

[9] S. J. Watts, J. Matheson, I. H. Hopkins-Bond, A. Holmes-Siedle, A. Mohammadzadeh, and R. Pace, "A new model for generation-recombination in silicon depletion regions after neutron irradiation," *IEEE Trans. Nucl. Sci.*, vol. 43, no. 6, pp. 2587–2594, Dec. 1996.

[10] K. Gill, G. Hall, and B. Macevoy, "Bulk damage effects in irradiated silicon detectors due to clustered divacancies," *J. Appl. Phys.*, vol. 82, pp. 126–136, Jul. 1997.

[11] S. Pellegrini, "Industrialised SPAD in 40 nm technology," in *IEDM Tech. Dig.*, San Francisco, CA, USA, Dec. 2018, p. 16.

[12] J. J. Liou, "Modeling the tunnelling current in reverse-biased p/n junctions," *Solid-State Electron.*, vol. 33, no. 7, pp. 971–972, Jul. 1990.

[13] J. M. Belloir, "Spectroscopie du courant d'obscurité induit par les effets de déplacement atomique des radiations spatiales et nucléaires dans les capteurs d'images CMOS à photodiode pincée," Ph.D. dissertation, Département Electronique Optronique et Signal, Univ. Toulouse, Toulouse, France, 2016.

[14] J. W. Palko and J. R. Srour, "Amorphous inclusions in irradiated silicon and their effects on material and device properties," *IEEE Trans. Nucl. Sci.*, vol. 55, no. 6, pp. 2992–2999, Dec. 2008.

[15] R. M. Fleming, D. V. Lang, C. H. Seager, E. Bielejec, G. A. Patrizi, and J. L. Campbell, "Continuous distribution of defect states and band gap narrowing in neutron irradiated GaAs," *J. Appl. Phys.*, vol. 107, Jun. 2010, Art. no. 123710.

[16] T. Nuns, G. Quadri, J. P. David, and O. Gilard, "Annealing of proton-induced random telegraph signal in CCDs," *IEEE Trans. Nucl. Sci.*, vol. 54, no. 4, pp. 1120–1128, Aug. 2007.

[17] A. Jay et al., "Simulation of single particle displacement damage in silicon–Part II: Generation and long-time relaxation of damage structure," *IEEE Trans. Nucl. Sci.*, vol. 64, no. 1, pp. 141–148, Jan. 2017.

[18] A. Jay et al., "Simulation of single-particle displacement damage in silicon—Part III: First principle characterization of defect properties," *IEEE Trans. Nucl. Sci.*, vol. 65, no. 2, pp. 724–731, Feb. 2018.